Sensitivity of two-fragment correlation functions to initial-state momentum correlations

R. Popescu, T. Glasmacher, J. D. Dinius,* S. J. Gaff, C. K. Gelbke, D. O. Handzy,[†] M. J. Huang, G. J. Kunde,[‡] W. G. Lynch,
L. Martin,[§] C. P. Montoya,[‖] and M. B. Tsang

Department of Physics and Astronomy and National Superconducting Cyclotron Laboratory,
Michigan State University, East Lansing, Michigan 48824-1321

N. Colonna, L. Celano, and G. Tagliente
INFN, Bari, Italy

G. V. Margagliotti, P. M. Milazzo, R. Rui, and G. Vannini
Dipartimento di Fisica and INFN, Trieste, Italy

M. Bruno, M. D'Agostino, and M. L. Fiandri
Dipartimento di Fisica and INFN, Bologna, Italy

F. Gramegna
INFN, Laboratori Nazionali di Legnaro, Italy

A. Ferrero,[¶] I. Iori, A. Moroni, and F. Petruzzelli
Dipartimento di Fisica and INFN, Milano, Italy

P. F. Mastinu
Dipartimento di Fisica, Padova, Italy,
and INFN, Bologna, Italy

L. Phair and K. Tso
Nuclear Science Division, Lawrence Berkeley National Laboratory, Berkeley, California 94720

(Miniball/Multics Collaboration)
(Received 15 September 1997)

Two-fragment reduced-velocity correlation functions were measured for small-impact-parameter collisions of ^{86}Kr $+^{93}$Nb at $E/A = 50$ MeV and compared to results of many-body Coulomb-trajectory calculations performed for instantaneous and sequential multifragment breakup scenarios. The correlation functions indicate emission on a very short time scale and appear consistent with an instantaneous breakup scenario, even though they exhibit a pronounced dependence on fragment kinetic energy when fragments are emitted at large transverse momenta. For the case of instantaneous breakup, sensitivities to initial-state momentum correlations due to total momentum conservation and to different emission patterns are investigated. For fragments emitted with large transverse momenta, momentum conservation constraints can cause a dependence of reduced-velocity correlation functions on fragment energy and fragment charge similar to those observed experimentally. [S0556-2813(98)04707-4]

PACS number(s): 25.70.Pq

I. INTRODUCTION

Highly excited nuclear systems formed in intermediate-energy heavy-ion collisions disintegrate by multifragment breakup [1,2]. Statistical treatments of multifragment decays are either based upon the assumption of an instantaneous breakup [3–5] of an expanded, highly excited nuclear system or, alternatively, a sequence of binary emissions with complete equilibration between decay steps [6–8]. However, even in the sequential decay approximation, multifragment emission is predicted to occur over a short time interval ($\tau < 100$ fm/c) when the nuclear system has expanded to subnormal density [7,8]. Microscopic calculations performed with the Boltzmann-Uehling-Uhlenbeck (BUU) transport model indicate that nonspherical or even noncompact source configurations may play an important role at the late, low-density stage of small-impact-parameter nucleus-nucleus collisions [9–15]. It is thus important to develop methods which are sensitive to the time scale and source configuration of the multifragment breakup phase.

Information about source dimensions and emission time scales can be obtained by studying final-state interactions between emitted fragments. Most significantly, the Coulomb repulsion between the emitted fragments leads to a depletion of the phase space at small relative momenta which can be observed as a suppression of the two-fragment correlation function at small relative velocities [16–31]. The width of this ''Coulomb hole'' increases when fragments are emitted in closer proximity, i.e., from smaller sources and/or over shorter time intervals. Using this technique, studies of two-fragment correlation functions revealed that fragment emission in central collisions occurs over a short time interval ($\tau < 200$ fm/c) [18–26]. In several cases, the assumption of an instantaneous breakup of an expanded source provides a satisfactory description of the data [27–30].

Dependences of the correlation functions on the energy of the emitted fragments [23–25] contain information which may help discriminate between instantaneous breakup and sequential emission. In addition, directional correlation functions have been shown to depend on the shape of the emitting source [31]. Evaporation models [6–8] predict higher fragment emission rates and, on average, higher fragment energies during the early stages of the decay chain when the source temperature is high. Thus, for rapidly emitted high-energy fragments, the Coulomb hole in the two-fragment correlation function should be wider than for low-energy fragments which emerge at a later stage of the reaction where the temperature and emission rate are reduced. Increasing widths of the Coulomb hole for fragment pairs of higher energy can thus signal emission from a cooling and possibly expanding source. Indeed, recent observations of such an energy dependence [23–25] could be described by a sequential picture with fragment emission occurring over short time intervals ($0 < \tau \leq 150$ fm/c). In some cases, emission times as short as a few tens of fm/c were extracted for which the distinction between sequential and instantaneous emission becomes tenuous and systematic uncertainties may need reassessment.

In this paper, we investigate two-fragment reduced-velocity correlation functions measured for small-impact-parameter collisions of ^{86}Kr $+ ^{93}$Nb at $E/A = 50$ MeV. For fragments emitted at large transverse momenta, the experimental two-fragment correlation function exhibits an unusual shape which strongly depends on fragment energy and element number. In order to provide a qualitative understanding of this behavior, we explore the sensitivity of calculated two-fragment correlation functions to different reasonable, but unknown initial conditions. Our calculations are consistent with an instantaneous breakup scenario ($\tau \to 0$). In this limit, uncertainties arise from unknown initial-state momentum correlations due to momentum conservation constraints. Such constraints can lead to energy-dependent two-fragment correlation functions and a loss of the approximate scaling [18] of two-fragment correlation functions with the ''reduced'' relative velocity of two fragments, $\mathbf{v}_{\mathrm{red}} = \mathbf{v}_{\mathrm{rel}}/(Z_1 + Z_2)^{1/2}$.

II. EXPERIMENTAL DETAILS

The experiment was performed at the National Superconducting Cyclotron Laboratory at Michigan State University.

The ^{86}Kr^{36+} beam had an intensity of 3×10^7 particles per second, and the ^{93}Nb target had an areal density of 2 mg/cm^2. Charged particles with element number $Z \leq Z_{\mathrm{projectile}}$ emitted at $3° \leq \theta_{\mathrm{lab}} \leq 23°$ were detected and identified with the ''Multics'' high-resolution array [32]. Fragments with $Z \leq 20$ emitted at $23° \leq \theta_{\mathrm{lab}} \leq 160°$ were detected by 171 phoswich detector elements of the MSU Miniball [33]. The geometric acceptance of the combined array was greater than 87% of 4π. The charge identification thresholds in the Miniball were $E_{\mathrm{th}}/A \approx 2$, 3, and 4 MeV for $Z = 3$, 10, and 18, respectively, and $E_{\mathrm{th}}/A \approx 1.5$ MeV in the Multics array, independent of the fragment charge.

We analyzed reduced-velocity correlation functions for intermediate-mass fragments (IMF's) of element number $4 \leq Z_{\mathrm{IMF}} \leq 9$ detected at $5° \leq \theta_{\mathrm{lab}} \leq 50°$. Small-impact-parameter collisions were selected by a cut on the detected charged particle multiplicity, $N_C \geq 20$. In a sharp cutoff approximation [34], this cut corresponds to a reduced impact parameter of $b/b_{\mathrm{max}} \leq 0.3$.

Digitization effects caused by the finite granularity of the Miniball detectors were reduced by assigning each detected fragment a random emission angle lying within the geometric boundary of the detector hit by the fragment. The probability distribution was chosen to produce a uniform hit pattern over the detector surface.

Consistent with previous work, the reduced-velocity two-fragment correlation function is defined as [18]

$$1 + R(v_{\mathrm{red}}) = C \frac{N_{\mathrm{corr}}(v_{\mathrm{red}})}{N_{\mathrm{uncorr}}(v_{\mathrm{red}})}, \qquad (1)$$

where v_{red} represents the reduced velocity [18] of the pair,

$$\mathbf{v}_{\mathrm{red}} = \frac{(\mathbf{p}_1/m_1 - \mathbf{p}_2/m_2)}{\sqrt{Z_1 + Z_2}}. \qquad (2)$$

Here, $\mathbf{p}_i$, m_i, and Z_i are, respectively, the momentum, mass, and charge of fragment i; $N_{\mathrm{corr}}(v_{\mathrm{red}})$ is the measured coincidence yield and $N_{\mathrm{uncorr}}(v_{\mathrm{red}})$ is the ''background yield'' constructed by using fragments from different events [35]. The normalization constant C is chosen such that the average correlation function $\langle 1 + R \rangle$ is unity for large reduced velocities where final-state interactions between fragments are small. Specifically, we chose $\langle R \rangle = 0$ over the interval $0.05 \leq v_{\mathrm{red}}/c \leq 0.07$ for $5° \leq \theta_{\mathrm{lab}} \leq 25°$ and $0.07 \leq v_{\mathrm{red}}/c \leq 0.09$ for $25° \leq \theta_{\mathrm{lab}} \leq 50°$. Other normalization prescriptions exist and are used by various groups. Our qualitative conclusions are independent of the particular choice of normalization as long as calculations and data are normalized consistently.

In order to study dependences on energy and emission angle of the coincident fragment pairs, we constructed correlation functions for two cuts on the center-of-mass energy, $E_{\mathrm{c.m.},i}/A_i \geq 3$ MeV and $E_{\mathrm{c.m.},i}/A_i \geq 7$ MeV, and for two cuts on the laboratory emission angle, $5° \leq \theta_{\mathrm{lab}} \leq 25°$ and $25° \leq \theta_{\mathrm{lab}} \leq 50°$. The two angular cuts have different phase space acceptances: the small-angle cut accepts preferentially longitudinal correlations, $\mathbf{v}_{\mathrm{red}} \| (\mathbf{p}_1 + \mathbf{p}_2)$, and the large-angle cut accepts preferentially transverse correlations, $\mathbf{v}_{\mathrm{red}} \perp (\mathbf{p}_1 + \mathbf{p}_2)$.
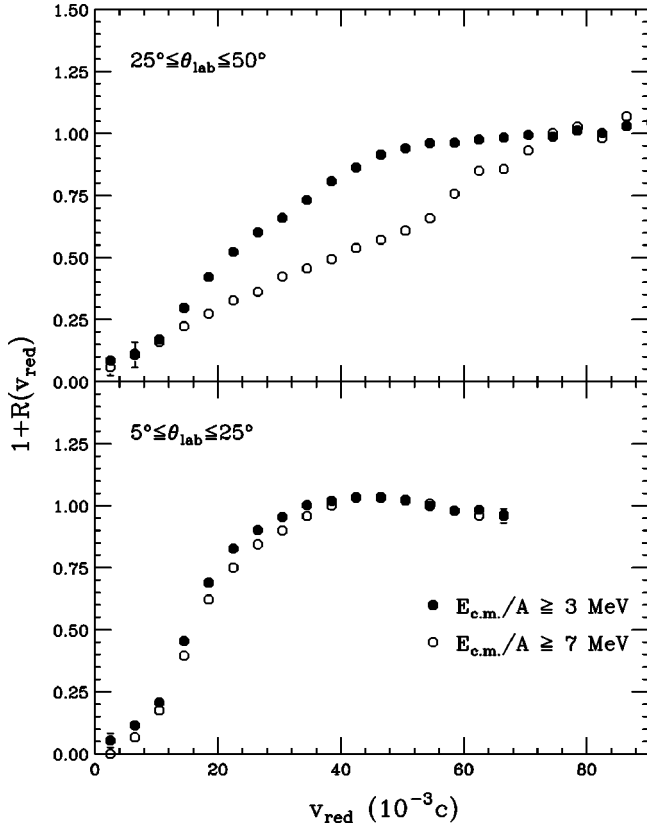
FIG. 1. Two-fragment correlation functions, integrated over all fragment pairs with element numbers $4 \leq Z_{IMF} \leq 9$, for small-impact-parameter collisions of $^{86}Kr + ^{93}Nb$ at $E/A = 50$ MeV. The top and bottom panels show data for fragments emitted at $25° \leq \theta_{lab} \leq 50°$ and $5° \leq \theta_{lab} \leq 25°$, respectively. Solid and open points show the results for low and high cuts on the fragments center-of-mass energy, $E_{c.m.,i}/A_i \geq 3$ MeV and $E_{c.m.,i}/A_i \geq 7$ MeV, respectively. Statistical error bars smaller than the size of the data points are not shown.

III. EXPERIMENTAL CORRELATION FUNCTIONS

Two-fragment correlation functions integrated over all fragment pairs with element numbers $4 \leq Z_{IMF} \leq 9$ are shown
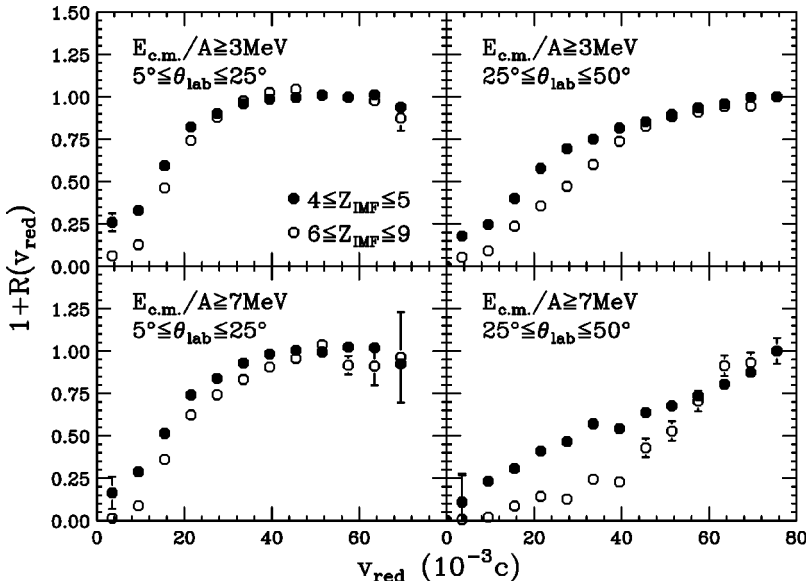
in Fig. 1. The top and bottom panels show correlation functions at large ($25° \leq \theta_{lab} \leq 50°$) and small ($5° \leq \theta_{lab} \leq 25°$) angles, respectively. Solid and open points show the results for the low- ($E_{c.m.,i}/A_i \geq 3$ MeV) and high- ($E_{c.m.,i}/A_i \geq 7$ MeV) energy thresholds, respectively. For fragments observed at large polar angles, the measured two-fragment correlation function exhibits a strong dependence on the minimum fragment energy, similar to previous observations [20,23–25]. In contrast, the energy dependence of the two-fragment correlation function is small at forward angles. The shape of the correlation function at forward angles is similar to the shapes observed in many other experiments [18–26], exhibiting a pronounced Coulomb hole at small reduced velocities and a rather flat region at larger reduced velocities. In contrast, the high-energy correlation function at larger angles exhibits a rather unusual shape with no well-defined flat region at large reduced velocities (top panel, open circles).

Two-fragment correlation functions for two groups of fragments, $4 \leq Z_{IMF} \leq 5$ (solid points) and $6 \leq Z_{IMF} \leq 9$ (open points), are shown in Fig. 2. The left and right panels show correlation functions for fragments emitted at small ($5° \leq \theta_{lab} \leq 25°$) and large ($25° \leq \theta_{lab} \leq 50°$) angles, respectively. Top and bottom panels show results for low and high cuts on the center-of-mass energy, $E_{c.m.,i}/A_i \geq 3$ MeV and $E_{c.m.,i}/A_i \geq 7$ MeV, respectively. Consistent with previous observations [18], the correlation function at forward angles and for the low-energy threshold exhibits a relatively weak dependence on Z_{IMF}. In contrast, the shape of the correlation function depends rather strongly on Z_{IMF} for fragments emitted at larger angles and with higher energy.

Reduced-velocity correlation functions independent of fragment charge are expected [18] when the two-fragment correlation function is largely determined by the two-fragment Coulomb interaction and when the fragment emission time scale does not depend on Z_{IMF}. A strong dependence of $R(v_{red})$ on Z_{IMF} indicates that at least one of these two assumptions is invalid.

IV. COMPARISON TO MANY-BODY COULOMB-TRAJECTORY CALCULATIONS

In this section, we compare the measured two-fragment correlation functions with predictions of many-body

FIG. 2. Two-fragment correlation functions for two groups of fragments, $4 \leq Z_{IMF} \leq 5$ (solid points) and $6 \leq Z_{IMF} \leq 9$ (open points) for small-impact-parameter collisions of $^{86}Kr + ^{93}Nb$ at $E/A = 50$ MeV. Left and right hand panels show correlation functions for fragments detected at $5° \leq \theta_{lab} \leq 25°$ and $25° \leq \theta_{lab} \leq 50°$, respectively. Top and bottom panels show the results for low- and high-fragment-energy thresholds $E_{c.m.,i}/A_i \geq 3$ MeV and $E_{c.m.,i}/A_i \geq 7$ MeV, respectively. Statistical error bars are only shown when they exceed the size of the data points.

Coulomb-trajectory calculations. Unless stated otherwise, the calculations are filtered by the acceptance of the experimental apparatus. The calculations are aimed at exploring uncertainties arising from various assumptions about the initial-state configurations and at illustrating physical conditions which may give rise to the qualitative features observed in the experimental correlation functions.

The determination of the ''true'' source configuration and lifetime from experimental correlation functions represents a difficult inversion problem which has only recently been attacked for the case of light-particle intensity interferometry when final-state interactions with the source are negligible [36]. For two-fragment correlation functions, which depend on many-body Coulomb interactions, the corresponding inversion problem has not yet been solved.

For simplicity, we will explore to what extent emission from a single spherical source can account for the observed experimental features. This simplifying assumption may, however, not be entirely realistic. For example, our impact parameter selection may not be sufficiently tight to completely eliminate contamination from spectator sources produced in collisions with a nonzero impact parameter. Even in strictly central collisions, noncompact and/or nonspherical sources can occur. For instance, microscopic simulations with the BUU transport theory have predicted [9–15] the occurrence of noncompact toroidal decay configurations in central collisions of nuclei with masses and energies comparable to the present experiment. Thus, we will not attempt to determine a unique set of source parameters, and some discrepancies between calculations and data may remain unresolved.

A. Sequential decay

Sequential decay calculations were performed for a source of fixed radius R_S, initially at rest in the center-of-mass frame and containing Z_{tot} protons; the initial mass of the source, M_{tot}, was taken as that of the most abundant isotope. After each emission, charge and mass of the emitted IMF were subtracted from the source, but the radius was kept fixed for simplicity. Charge distributions of the emitted fragments ($3 \leqslant Z_{IMF} \leqslant 20$) were generated by randomly sampling the experimental yield distribution; the total charge $Z_{tot,IMF}$ removed by all emitted IMF's was a model parameter which controlled the IMF multiplicity distribution. For a given charge number Z_{IMF}, the mass number A_{IMF} of the emitted IMF was chosen as that of the most abundant isotope and its radius to be $R_{IMF}=1.2(A_{IMF})^{1/3}$ fm. (This assumption on fragment mass introduces a small uncertainty in the determination of source parameters [37], but it does not affect our qualitative conclusions.) For each IMF, we generated a momentum vector isotropically in the frame of the emitting source; the IMF energies were chosen to reproduce the experimental fragment energy distribution in the center-of-mass system.

The fragment emission times t_i were assumed to have the probability distribution $P(t) \propto e^{-t/\tau}$. Recoil velocity and mass conservation of the source were taken into account for each subsequent emission. (The case of instantaneous disintegration, $\tau \to 0$, is discussed separately below.) The source radius was kept fixed as $R_S=9$ fm, and the centers of the

fragments were initially placed at the distance of $r=R_S+R_{IMF}$ from the center of the source, requiring outward emission, $\mathbf{r} \cdot \mathbf{p} \geqslant 0$. (Here, $\mathbf{r}$ is the position vector of the IMF with respect to the center of the source and $\mathbf{p}$ is the momentum vector in the recoiling rest frame.) Consistent with previous work, the surface emission pattern from point $\mathbf{r}$ was assumed [18] to follow Lambert's law, $P(\alpha) \propto \cos \alpha = (\mathbf{r} \cdot \mathbf{p})/(rp)$, where α is the angle between the normal to the surface, $\hat{\mathbf{n}}=\mathbf{r}/r$, and the velocity of the emitted particle. Thus the probability distribution for initial positions $\mathbf{r}_i$ and momenta $\mathbf{p}_i$ was taken as

$$P(\mathbf{r}_i, \mathbf{p}_i) \propto P(p_i) \theta(\mathbf{r}_i \cdot \mathbf{p}_i) \delta(r_i - R_S - R_{IMF,i})$$
$$\times (\mathbf{r}_i \cdot \mathbf{p}_i)/(r_i p_i), \qquad (3)$$

where $\theta(x)$ is the unit step function which vanishes for negative arguments, and $P(p_i)$ is the assumed single-particle momentum distribution, assumed to be isotropic in the source frame, $P(p_i)=P(m_i v_i)$, and taken as the angle-integrated experimental center-of-mass distribution of fragment i, corrected for the average Coulomb repulsion from the source. In this approximation, the initial momentum p_i is related to the final momentum $p_{f,i}$ according to

$$p_i = \sqrt{p_{f,i}^2 - 2m_i E_{Coul,i}} \qquad (4)$$

where $E_{Coul,i}=e^2 Z_i(Z_{tot}-Z_i)/(R_S+R_{IMF})$. The distribution of momenta $p_{f,i}$ was randomly sampled from the experimental (angle-integrated) momentum distribution in the source rest frame. Initial configurations with overlapping fragments were rejected. After initialization, the Coulomb-trajectory calculations were performed by assuming point particles.

The curves in Fig. 3 show the results of sequential decay calculations for fragments emitted at small ($5° \leqslant \theta_{lab} \leqslant 25°$, left hand panels) and large ($25° \leqslant \theta_{lab} \leqslant 50°$, right hand panels) angles, respectively. Top and bottom panels show the results for low- and high-energy thresholds, respectively. The different lifetimes τ assumed in the calculations are indicated in the figure. In these calculations, the parameters $Z_{tot}=70$, $R_S=9$ fm, and $Z_{tot,IMF}=32$ were used, and the same selections in charge, energy and polar angle were applied as in the experimental data. (For $Z_{tot,IMF}=32$, the average IMF multiplicity per simulated event is $\langle N_{IMF} \rangle \approx 6$.) For the assumed source geometry, satisfactory agreement with the data can be obtained by assuming emission on a very short time scale $\tau < 100$ fm/c [38]. Such a fast time scale is consistent with previous results from other investigations [18–30]. Since the assumption of a longer emission time scale increases the disagreement with the data, our remaining investigation will be performed for the zero lifetime limit $\tau = 0$.

B. Initial-state momentum correlations
for instantaneous decay

For sequential decay calculations, the implementation of momentum conservation is unambiguously determined by the assumed sequence of binary decays and the subsequent (momentum conserving) evolution of the Coulomb trajectories. For instantaneous disintegrations, the choice of an initial set of particle momenta $\mathbf{p}_i$ which satisfies $\mathbf{P}_{tot}=\Sigma \mathbf{p}_i=0$ is
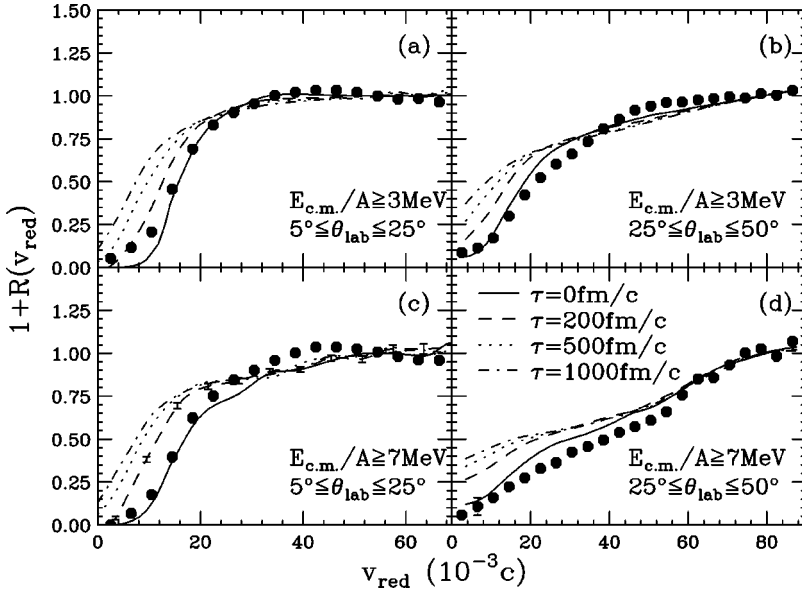
FIG. 3. The points show two-fragment correlation functions, integrated over all fragment pairs with $4 \leq Z_{IMF} \leq 9$ for $^{86}Kr + ^{93}Nb$ at $E/A = 50$ MeV. Left and right hand panels show correlation functions for fragments detected at $5° \leq \theta_{lab} \leq 25°$ and $25° \leq \theta_{lab} \leq 50°$, respectively. Top and bottom panels show the results for low- and high-fragment-energy thresholds $E_{c.m.,i}/A_i \geq 3$ MeV and $E_{c.m.,i}/A_i \geq 7$ MeV, respectively. The curves show the results of sequential decay calculations using the parameters $Z_{tot} = 70$, $R_S = 9$ fm, and $Z_{tot,IMF} = 32$, filtered by the experimental acceptance. The assumed lifetimes τ are labeled in the figure. Typical numerical uncertainties are indicated for a panel when significant, e.g., in panel (c) for the $\tau = 200$ fm/c calculation.

not uniquely determined, even if the single-particle momentum distribution is assumed to be known. In our investigation of instantaneous decay, we used three prescriptions for the initialization of IMF momenta. One prescription corresponds to the short-lifetime limit $\tau \rightarrow 0$ of sequential emission from the surface of an excited source (dubbed the *sequential* approximation). Another prescription (dubbed the *rescaling* approximation) eliminates the velocity of the center of mass for each set of randomly selected particle momenta [39]. A third prescription (dubbed the *residue* approximation) assumes that the momentum balance is taken up by the residue.

In all cases, the initial source was assumed to be at rest in the center-of-mass frame of projectile and target, and the initialization of particle positions was treated identically. As before, a source of fixed radius R_S, initial charge number Z_{tot}, and initial mass M_{tot} was assumed. The IMF charge and mass distributions and their initial positions with respect to the center of the source were sampled as described in the previous section.

In the *sequential* approximation, the fragment momenta were chosen one after the other. After each choice, the residual source received a recoil velocity according to momentum conservation. Recoil velocity and mass conservation were taken into account for each subsequent emission, but the source location was kept fixed during the initialization ($\tau \rightarrow 0$ limit). In the center-of-mass frame, the velocity $\mathbf{v}_i$ of the ith fragment is thus

$$\mathbf{v}_i = \mathbf{v}'_i + \mathbf{V}_{i-1}. \quad (5)$$

Here, $\mathbf{V}_0 = 0$ denotes the velocity of the initial source of mass $M_0 = M_{tot}$. After emission of fragment i, the residual source has the velocity $\mathbf{V}_i = \mathbf{V}_{i-1} - m_i \mathbf{v}'_i/M_i$ and the mass $M_i = M_{i-1} - m_i$, where $\mathbf{v}'_i$ is the velocity of fragment i with respect to the rest frame of the emitting source of mass M_{i-1} and $\mathbf{v}'_i$ is selected according to the probability distribution $P(\mathbf{r}_i, m_i \mathbf{v}'_i)$, given by Eq. (3). In this approximation, Lambert's law is applied to the selection of $\mathbf{v}'_i$, i.e., with respect to the center and rest frame of the $(i-1)$th residue of mass M_{i-1} and velocity $\mathbf{V}_{i-1}$.

Alternatively, one could also select the velocities $\mathbf{v}'_i$ by sampling an isotropic distribution $P(m_i v'_i)$ by implementing momentum conservation according to Eq. (5) and by then selecting the initial positions such that Lambert's law is satisfied in the rest frame of the original source. In principle, this latter approximation differs from the $\tau \rightarrow 0$ limit of the sequential decay discussed in the previous section. However, the calculations were found to be insensitive to such detail and these two prescriptions gave virtually indistinguishable results.

In the *rescaling* approximation, a set of initial IMF momenta $\mathbf{p}'_i$ was randomly chosen from an isotropic probability distribution $P(p'_i)$. After selection of all IMF momenta $\mathbf{p}'_i$, the momentum of the residue was chosen as $\mathbf{p}'_{res} = 0$. In order to conserve momentum in the source rest frame, all momenta ($\mathbf{p}'_i$ and $\mathbf{p}'_{res}$) were shifted so that the total momentum was zero:

$$\mathbf{p}_i = \alpha \left\{ \mathbf{p}'_i - \left(\sum_j \mathbf{p}'_j \right) \frac{m_i}{M_{tot}} \right\}. \quad (6)$$

Here, the indices i and j label all particles (including the residue). The factor α is chosen to ensure energy conservation,

$$\sum_i \frac{\mathbf{p}'^2_i}{2m_i} = \sum_i \frac{\mathbf{p}^2_i}{2m_i}. \quad (7)$$

In the present context, the scale factor α is largely cosmetic; setting $\alpha = 1$ makes the simulated energy spectra slightly steeper than the original single-particle spectrum, but this has negligible effects on the correlation function. The rescaled momenta $\mathbf{p}_i$ were then taken as the initial momenta for the many-body Coulomb-trajectory calculations from which the final particle momenta were calculated. For the selected set of rescaled fragment momenta $\mathbf{p}_i$, the initial positions were randomly chosen under the constraint that Lambert's law be satisfied for a sphere at rest in the center-
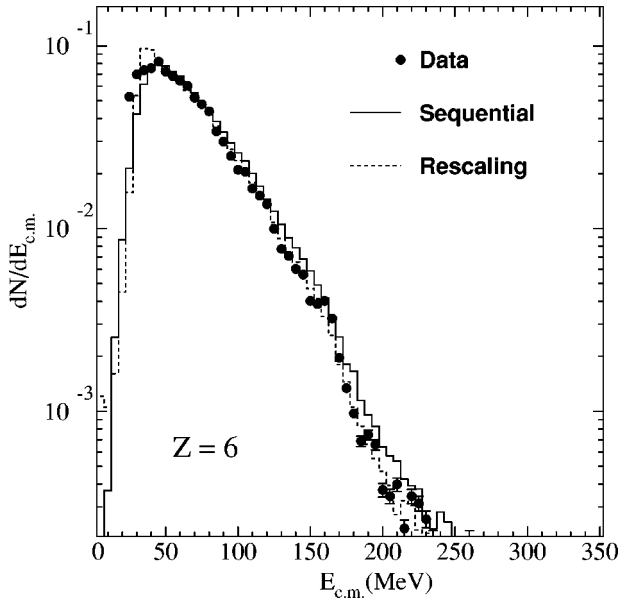
FIG. 4. Angle-integrated center-of-mass energy distribution of carbon fragments. Experimental data are shown as points; solid and dashed curves show the single-particle spectra obtained with the sequential and rescaling approximations.

of-mass frame. The initial fragments were placed at the radius $R = R_S + R_{IMF}$, and initial configurations with overlapping fragments were rejected.

In the *residue* approximation, the initial fragment momenta $\mathbf{p}_i$ were chosen randomly from the isotropic probability distribution $P(p_i)$. Momentum conservation was implemented by imparting a momentum $\mathbf{p}_{res} = -\Sigma \mathbf{p}_i$ to the residual source, and Lambert's law was implemented in the center-of-mass frame.

Upon initialization, all fragments were released simultaneously from the surface, and many-body Coulomb trajectories were calculated by assuming point particles. The reduced-velocity correlation functions were computed for fragment pairs filtered by the experimental acceptance and the applied software cuts.

For illustration, Fig. 4 compares the measured and calcu-

lated (angle-integrated) center-of-mass energy distribution of carbon fragments. Per construction, both calculations reproduce the energy spectra of emitted fragments reasonably well. [In the sequential approximation, the high-energy part of the energy spectrum is slightly overpredicted. This effect is due to second- and later-chance emissions from the recoiling source. This discrepancy is inconsequential for the calculation of the correlation function, but could be trivially eliminated, e.g., by multiplying the momenta by a factor of α to ensure energy conservation analogous to Eqs. (6) and (7).] Differences between correlation functions predicted by the different momentum conservation methods are not caused by slight differences in the single-particle energy distributions.

Predictions for instantaneous decay are shown in Fig. 5. The points show experimental two-fragment correlation functions, integrated over all fragment pairs with $4 \leq Z_{IMF} \leq 9$ for $^{86}Kr + ^{93}Nb$ at $E/A = 50$ MeV. Left and right hand panels show correlation functions for fragments detected at $5° \leq \theta_{lab} \leq 25°$ and $25° \leq \theta_{lab} \leq 50°$, respectively. Top and bottom panels show the results for low- and high-fragment-energy thresholds $E_{c.m.,i}/A_i \geq 3$ MeV and $E_{c.m.,i}/A_i \geq 7$ MeV, respectively. The curves show correlation functions calculated for instantaneous breakup using three different prescriptions for total initial momentum conservation. As in Fig. 3, the parameters $Z_{tot} = 70$, $R_S = 9$ fm, and $Z_{tot,IMF} = 32$ were used, and the same selections in charge, energy, and polar angle were applied as in the experimental data.

Overall, all three calculations reproduce the forward angle data reasonably well (left panels of Fig. 5). At larger angles (right panels of Fig. 5), the *sequential* and *rescaling* approximations provide reasonable agreement with the data, but the *residue* approximation does not.

Even though all particles are released instantaneously and from a fixed geometry, the correlation functions are predicted to depend on fragment energy. The predicted energy dependence is particularly pronounced for the large-angle cut (right panels of Fig. 5). Energy-dependent two-fragment correlation functions are thus not unique proof of a time-ordered (sequential) emission process.

Because of the lack of position-sensitive detectors in the Miniball Array, the instrumental distortions are largest for
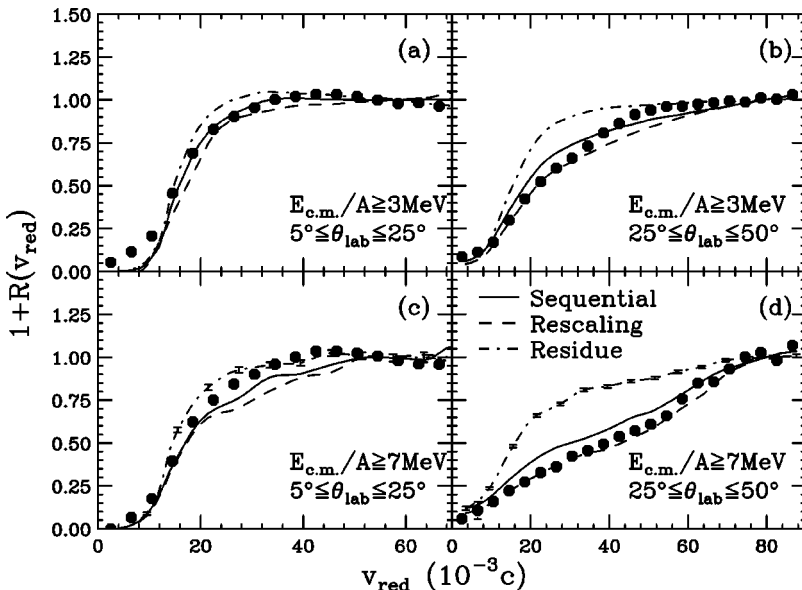

FIG. 5. The points show two-fragment correlation functions, integrated over all fragment pairs with $4 \leq Z_{IMF} \leq 9$ for $^{86}Kr + ^{93}Nb$ at $E/A = 50$ MeV. Left and right hand panels show correlation functions for fragments detected at $5° \leq \theta_{lab} \leq 25°$ and $25° \leq \theta_{lab} \leq 50°$, respectively. Top and bottom panels show the results for low- and high-fragment-energy thresholds $E_{c.m.,i}/A_i \geq 3$ MeV and $E_{c.m.,i}/A_i \geq 7$ MeV, respectively. The curves show correlation functions calculated for instantaneous breakup using three different prescriptions for total initial momentum conservation. As in Figs. 3 and 4, the parameters $Z_{tot} = 70$, $R_S = 9$ fm, and $Z_{tot,IMF} = 32$ were used. The calculations were filtered by the response of the experimental apparatus and by the experimental cuts on charge, energy, and polar angle. Typical numerical uncertainties are indicated for a panel when significant.
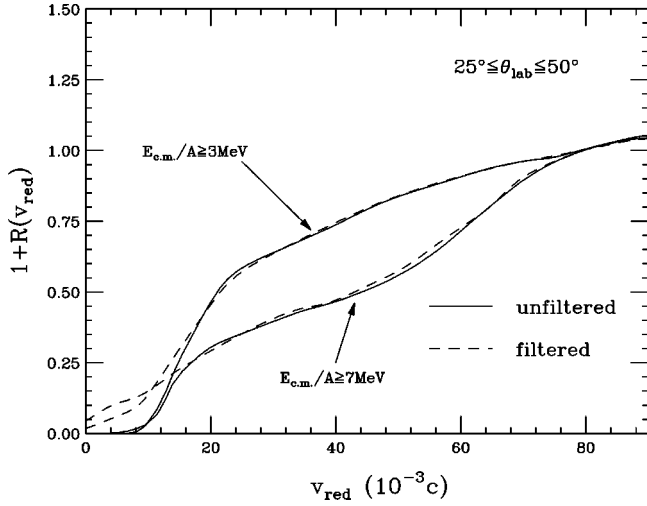
FIG. 6. Illustration of instrumental distortions of correlation functions at $25° \le \theta_{\mathrm{lab}} \le 50°$. Solid and dashed curves show unfiltered and filtered correlation functions calculated for the case of instantaneous breakup in the rescaling approximation.

the large-angle cut $25° \le \theta_{\mathrm{lab}} \le 50°$. The magnitude of the distortions is illustrated in Fig. 6 for the example of instantaneous decay calculated in the rescaling approximation. The unfiltered correlation functions are shown by solid curves and the filtered correlation functions are represented by dashed curves. As can be readily seen, the instrumental distortions of the calculated correlation functions are large for very small reduced velocities $v_{\mathrm{red}} < 0.02c$, but they become insignificant for larger reduced velocities $v_{\mathrm{red}} > 0.02c$. While important for quantitative comparisons between measured and calculated correlation functions, these experimental acceptance effects do not alter the general conclusions reached in the present investigation, namely, that (1) the correlation functions at large angles exhibit a strong dependence on particle energy and (2) this energy dependence is strongly influenced by (unknown) initial-state correlations due to momentum conservation constraints.

In order to demonstrate that the observed energy dependence is primarily due to the initial-state momentum correlations which arise from the different prescriptions of implementing momentum conservation for a finite system, we show in Fig. 7 the results of calculations in which the fragments are selected without momentum conservation constraints according to the single-particle probability, Eq. (3). In order to eliminate the (energy-dependent) effects of instrumental distortions, the calculations shown in Fig. 7 have not been filtered by the experimental resolution, but only by the energy and angular cuts indicated. In contrast to calculations which include initial-state momentum correlations (shown here for the rescaling approximation), the assumption of uncorrelated initial momenta produces correlation functions which are nearly energy independent. (Some minor energy dependence may be due to many-body Coulomb interactions, e.g., energy-dependent deflections in the Coulomb field of the heavy residue.)

The detailed results obtained with the three momentum initializations are surprisingly different, especially for two-fragment correlations at large angles and for high-energy thresholds, even though essential source parameters (size and
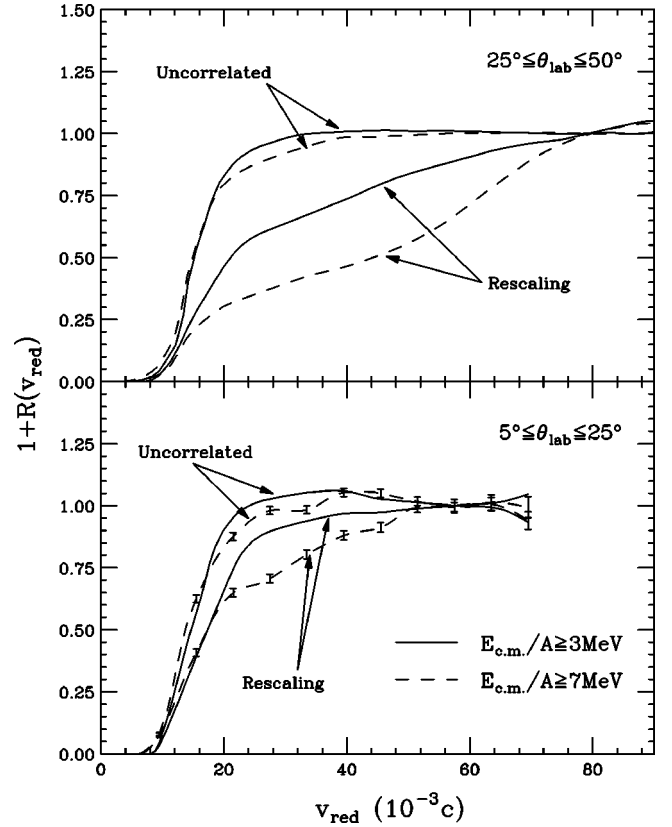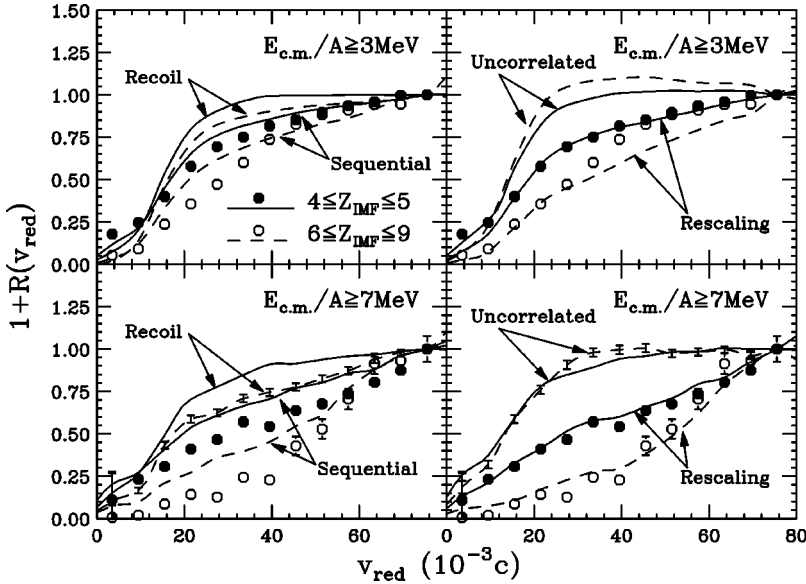

FIG. 7. The curves compare correlation functions calculated by selecting the initial fragment momenta according to the single-particle probability, Eq. (3), and neglecting initial-state momentum conservation effects (infinite-residue-mass limit, labeled as ''uncorrelated'') or, alternatively, by incorporating momentum conservation constraints in the rescaling approximation. Top and bottom panels show results for $25° \le \theta_{\mathrm{lab}} \le 50°$ and $5° \le \theta_{\mathrm{lab}} \le 25°$, respectively. Solid and dashed curves show the results for low- and high-fragment-energy thresholds $E_{\mathrm{c.m.},i}/A_i \ge 3$ MeV and $E_{\mathrm{c.m.},i}/A_i \ge 7$ MeV, respectively. In contrast to calculations shown in previous figures, the calculations shown here neglect instrumental resolution effects. Typical numerical uncertainties are indicated for a panel when significant.

lifetime) are identical. We conclude that the detailed shape of two-fragment correlation functions can be sensitive to initial-state momentum correlations. This sensitivity depends on the kinematic conditions under which the correlation function is constructed.

Since initial-state momentum correlations due to momentum conservation can strongly depend on the reaction dynamics, they are not known *a priori* and may be difficult (if not impossible) to extract from the single-particle spectra. Unless constrained by additional observations, such initial-state correlations can render the extraction of source parameters more ambiguous in the limit of instantaneous decay. Note, however, that the implementation of momentum conservation for truly *sequential decay is unambiguous*.

Initial-state momentum correlations due to momentum conservation constraints can affect the reduced-relative-velocity scaling [18] of two-fragment correlations. A unique dependence of two-fragment correlation functions on the reduced relative velocity, Eq. (2), should exist [18] if the two-fragment correlation function is dominated by the mutual

FIG. 8. Two-fragment correlation functions for ^{86}Kr$+^{93}$Nb and $E/A=50$ MeV, integrated over all fragment pairs at $25°\leqslant\theta_{lab}\leqslant50°$ with $4\leqslant Z_{IMF}\leqslant5$ (solid points, solid curves) and $6\leqslant Z_{IMF}\leqslant9$ (open points, dashed curves). Points show data; curves show calculations for instantaneous decay using the momentum initialization prescription indicated. Top and bottom panels show the results for low- and high-fragment-energy thresholds $E_{c.m.,i}/A_i\geqslant3$ MeV and $E_{c.m.,i}/A_i\geqslant7$ MeV, respectively. As in Figs. 3 and 4, the parameters $Z_{tot}=70$, $R_S=9$ fm, and $Z_{tot,IMF}=32$ were used, and the same selections in charge, energy and polar angle were applied as in the experimental data. Because of a lack of statistics at high values of v_{red}, the correlation functions shown in this figure were normalized such that $\langle R\rangle=0$ over the interval $0.07\leqslant v_{red}/c\leqslant0.08$.

Coulomb interaction between the two detected fragments and if the space-time characteristics of the emitting system are independent of Z_{IMF} over the range considered. Approximate scaling of two-fragment correlation functions with v_{red} has been observed experimentally [18], and it is often used to increase the statistical accuracy of the correlation function by summing over a finite range of Z_{IMF}. In our experiment, a unique dependence of the two-fragment correlation function on v_{red}, independent of Z_{IMF}, is not observed, especially for fragments emitted at larger angles $25°\leqslant\theta_{lab}\leqslant50°$; see Fig. 2.

Figure 8 shows the two-fragment correlation functions at $25°\leqslant\theta_{lab}\leqslant50°$ for two groups of fragments, $4\leqslant Z_{IMF}\leqslant5$ and $6\leqslant Z_{IMF}\leqslant9$ (solid and open points, respectively), and for two energy cuts $E_{c.m.,i}/A_i\geqslant3$ MeV and $E_{c.m.,i}/A_i\geqslant7$ MeV (top and bottom panels, respectively). These correlation functions are compared to calculations performed with and without initial-state momentum conservation constraints (filtered by the experimental acceptance). The calculations show that initial-state momentum correlations can lead to a strong Z_{IMF} dependence of two-fragment correlation functions, with details depending on the approximation (*recoil*, *sequential*, or *rescaling*) used. While none of the calculations provides a perfect fit to the data, the predicted effect has the right magnitude, indicating that initial-state momentum correlations are likely to have a significant influence on the Z_{IMF} dependence of the two-fragment correlation function. Consistent with previous results [11], an approximate scaling with reduced velocity is predicted if initial-state momentum conservation constraints are neglected; see curves labeled ''uncorrelated'' in the right hand panels of Fig. 8. Thus, for the data shown in Fig. 8, distortions from many-body Coulomb interactions (beyond the two-fragment interaction) appear to be less important than distortions due to initial-state momentum correlations imposed by momentum conservation constraints. Unfortunately, the implementation of these constraints is not unique—which makes the investigation of instantaneous decay scenarios model dependent.

C. Sensitivity to local emission pattern

Classical trajectory calculations require the specification of both initial coordinates and initial velocities of the emitted

fragments; i.e., one must provide the velocity distribution for each source point. Usually one samples a single-particle source function; see, e.g., Eq. (3). Initial-state momentum correlations due to momentum conservation have been discussed in the previous subsection. Here, we investigate the sensitivity to the assumptions on the local surface emission pattern $P(\mathbf{r}_i,\mathbf{p}_i)$ and to simple initial-state position correlations introduced to disallow initial configurations with overlapping fragments. For simplicity and clarity of presentation, these calculations are not filtered by the resolution of the experimental apparatus, but only by the indicated gates on emission and energy threshold in the rest frame of the source.

In Fig. 9, we compare correlation functions calculated by initializing the fragment positions such that overlapping fragments are prohibited (labeled as ''excluded volume,'' solid curves) or, alternatively, allowed (labeled as ''no excluded volume,'' dashed curves). Both calculations were performed by using identical single-particle distributions, Eq. (3), and by implementing the rescaling approximation for the momentum initialization. Results for the small- and large-angle cuts are shown in the lower and upper panels, respectively. The results of the two calculations are very similar. For the present case, the requirement of initially nonoverlapping fragments appears to be an unimportant feature of our many-body Coulomb-trajectory calculations. This result is not surprising for the low-density case considered here: fragments block less than 10% of the surface of the source.

In many calculations, including those presented in this paper, a surface emission pattern according to Lambert's law is assumed [18]; see Eq. (3). In order to investigate the sensitivity to this assumption, we have performed calculations for different surface emission patterns. Specifically, we assumed isotropic outward radiation from each point at the surface of the source (shown by dashed curves in Fig. 10, labeled ''2π emission''),

$$P(\mathbf{r}_i,\mathbf{p}_i)\propto P(p_i)\theta(\mathbf{r}_i\cdot\mathbf{p}_i)\delta(r_i-R_S-R_{IMF,i}), \qquad (8)$$

or, alternatively, isotropic emission from each source point, allowing inward directed velocities (shown by dotted curves in Fig. 10, labeled ''4π emission''),
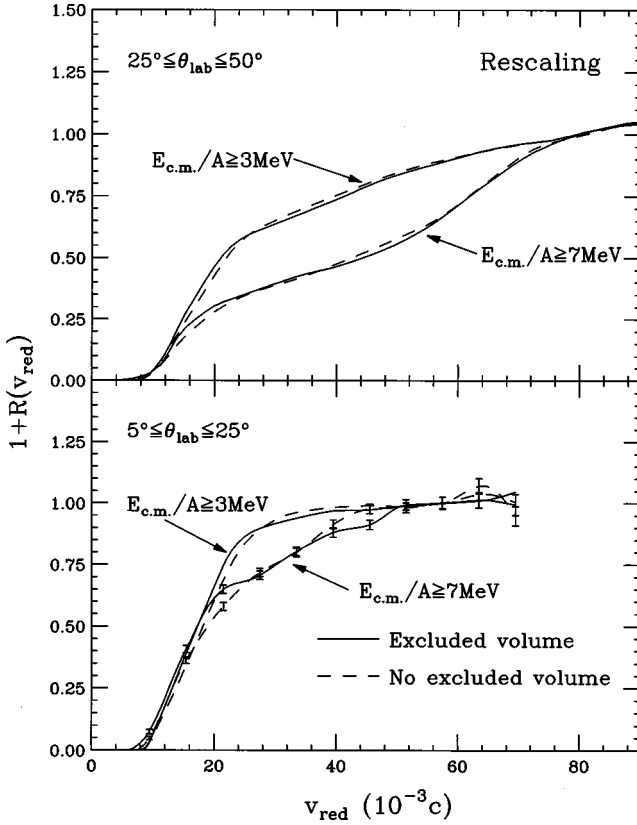
FIG. 9. Comparison of correlation functions calculated by allowing (dashed curves, labeled as ''no excluded volume'') or disallowing (solid curves, labeled as ''excluded volume'') initially overlapping fragment positions. The rescaling approximation was used to incorporate momentum conservation constraints. Top and bottom panels show results for $25° \leq \theta_{lab} \leq 50°$ and $5° \leq \theta_{lab} \leq 25°$, respectively. The energy cuts are indicated in the figure. Instrumental resolution effects are neglected. Typical numerical uncertainties are indicated for a panel when significant.

$$P(\mathbf{r}_i, \mathbf{p}_i) \propto P(p_i)\, \delta(r_i - R_S - R_{IMF,i}). \tag{9}$$

Calculations with these different surface radiation patterns are compared in Fig. 10. All calculations were performed by using identical source dimensions and by implementing the rescaling approximation for the momentum initialization. Results for the small- and large-angle cuts are shown in the lower and upper panels, respectively. While not identical, the results of the three calculations are very similar. Thus, the specific choice of surface emission function appears to be of minor importance.

D. Volume emission

Our calculations indicate that fragment emission occurs within a very short time interval, consistent with instantaneous breakup. These calculations were performed by assuming that fragments are released from the *surface* of a spherical source. This assumption of fragment release from the surface of the source is clearly reasonable for sequential fragment emission scenarios with complete equilibration between individual fragment emissions. However, for very short fragment emission time scales, and particularly for the
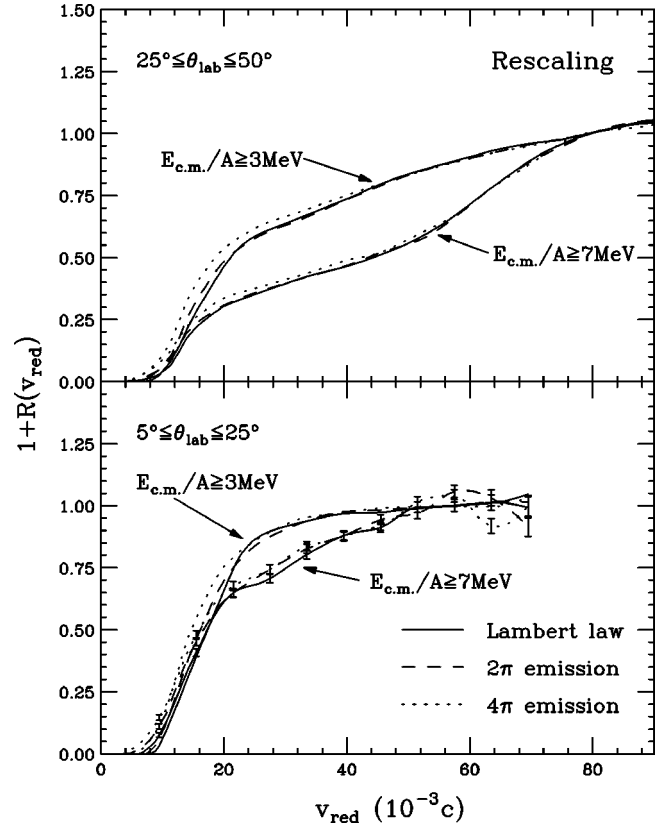
FIG. 10. Correlation functions predicted for different surface radiation patterns. Solid, dashed, and dotted curves represent calculations with the rescaling approximation ($\tau = 0$) using Eqs. (3), (8), and (9), respectively. Top and bottom panels show results for $25° \leq \theta_{lab} \leq 50°$ and $5° \leq \theta_{lab} \leq 25°$, respectively; the applied energy thresholds are given in the figure. Instrumental resolution effects are neglected. Typical numerical uncertainties are indicated for a panel when significant.

limiting case of instantaneous disintegration, fragment release from the volume of the source may be considered as a realistic alternative.

Thus, we have also performed calculations allowing for a random release of fragments from the *volume* of the source. These calculations are shown by the dashed and dotted curves in Fig. 11. For comparison, we also display the ''standard'' rescaling calculation for surface emission (solid curves in Fig. 11). After determining the position of the residual source, the initial fragment positions (i.e., the centers of the fragments) were chosen randomly within the spherical source volume (of radius $R_V = 12$ fm), under the constraint that initial fragments do not overlap geometrically. Two different prescriptions were explored as to the position of the residual source. In the calculations shown by the dashed curves (labeled ''residue in ct.''), the residue was placed at the center of the source volume, and in the calculations shown by dotted curves (labeled ''true volume''), the center of the residue was positioned randomly within the source volume. The initial fragment momenta $\mathbf{p}_i'$ were randomly chosen from an isotropic probability distribution $P(p_i')$, and momentum conservation constraints were imposed by means of the rescaling approximation, Eqs. (6) and (7).

Differences between volume and surface emission calculations are most pronounced for correlation functions corre-
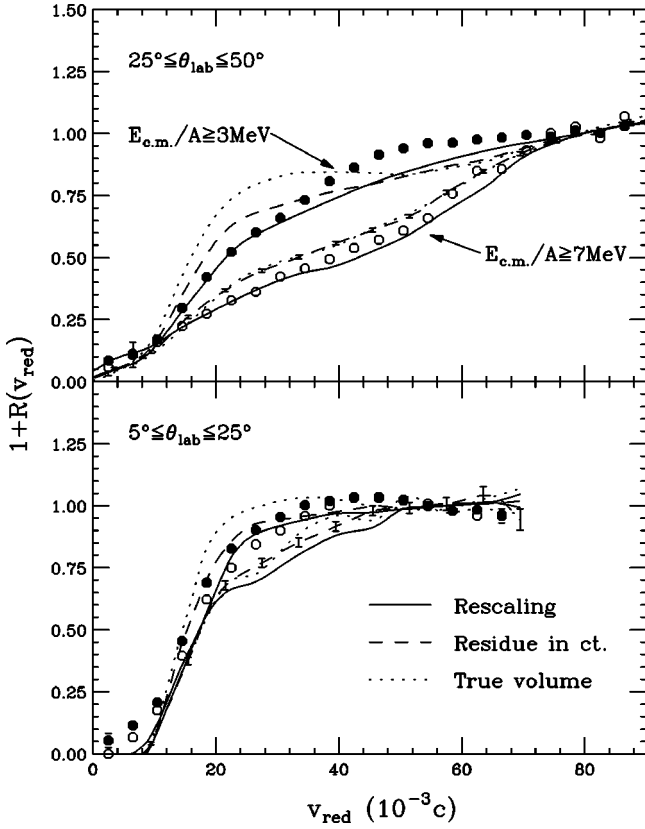
FIG. 11. The points show two-fragment correlation functions, integrated over all fragment pairs with $4 \leq Z_{IMF} \leq 9$ for ^{86}Kr $+ ^{93}$Nb at $E/A = 50$ MeV. Top and bottom panels show correlation functions for fragments detected at $25° \leq \theta_{lab} \leq 50°$ and $5° \leq \theta_{lab} \leq 25°$, respectively. Solid and open points show data for low- and high-fragment-energy thresholds, $E_{c.m.,i}/A_i \geq 3$ MeV and $E_{c.m.,i}/A_i \geq 7$ MeV, respectively. The dashed and dotted curves show the results of instantaneous breakup calculations assuming emission from a spherical volume of radius $R_S = 12$ fm, using the parameters $Z_{tot} = 70$ and $Z_{tot,IMF} = 32$. Solid curves show ''standard results'' for surface emission. The calculations are filtered by the experimental acceptance. Typical numerical uncertainties are indicated for a panel when significant.

sponding to the low-fragment-energy threshold $E_{c.m.,i}/A_i \geq 3$ MeV and large emission angles $25° \leq \theta_{lab} \leq 50°$; see top panel of Fig. 11. The difference is largest when the location of the residue is randomly chosen within the source volume since an off-center location of the residue results in a non-spherical distribution of the remaining fragments. The results of calculations with the residue positioned at the center of the source are more similar to those obtained for surface emission. Qualitatively, this can be understood as follows. If the residue is placed at the center of the source, the centers of the remaining fragments are distributed in a spherical shell of inner radius $R_{res} + R_{IMF} \approx 8$ fm and outer radius $R_V = 12$ fm. This distribution resembles emission from a diffuse surface. In our surface emission calculation, the fragment centers were located in a thin spherical shell at $R_S + R_{IMF} \approx 11$–12 fm.

The assumption of volume emission with the residue located at the center of the source provides comparable agreement with the data as the assumption of surface emission. The agreement is considerably worse if one assumes a ran-

dom location of the residue within the source volume.

The calculations show that the correlation functions are also sensitive to the spatial distribution of fragments within the source volume. This sensitivity is strongest for fragments emitted with low energy. However, this sensitivity to the spatial configuration cannot be trivially disentangled from the existing sensitivity to unknown correlations in the initial momentum distribution due to conservation laws.

V. SUMMARY AND CONCLUSIONS

We have measured reduced-velocity two-fragment correlation functions in small-impact-parameter ^{86}Kr $+ ^{93}$Nb collisions at $E/A = 50$ MeV and compared them to results of many-body Coulomb-trajectory calculations. Calculations for a sequential decay scenario indicate that fragment emission occurs over a short time interval ($\tau < 100$ fm/c), consistent with instantaneous decay. Assuming an instantaneous decay, we found little sensitivity of the calculated two-fragment correlation functions to details of the surface emission patterns. Correlation functions calculated for surface and volume emission were found to be different and sensitive to detailed assumptions regarding the location of the heavy residue. Reasonable agreement with the measured correlation functions could be obtained by assuming emission from the surface of the source. The data can also be reproduced reasonably well by assuming volume emission with the heavy residue placed at the center of the source; worse agreement with experiment was obtained when the location of the heavy residue was randomly distributed within the volume of the source.

The calculations were found to be rather sensitive to initial-state momentum correlations arising from momentum conservation constraints. Such constraints can produce energy-dependent correlation functions, with details depending on the experimental acceptance and on the particular method used to constrain the initial momenta. The predicted trends are similar to those observed experimentally. While the investigated methods of implementing momentum conservation constraints are reasonable, they are by no means unique because initial-state momentum correlations can depend on the reaction dynamics and are thus not known *a priori*. As a consequence, the extraction of source parameters from two-fragment correlation functions may be more model dependent than previously assumed.

Different from previous investigations, the reduced-velocity correlation functions observed in the present experiment exhibit a pronounced dependence on Z_{IMF}. Our calculations indicate that the reduced-velocity scaling should remain approximately valid if the fragments are emitted in a completely uncorrelated fashion and that the observed violation of reduced-velocity scaling cannot be entirely attributed to many-body Coulomb interactions. The calculations show further that initial-state momentum conservation constraints can lead to a strong dependence of the reduced velocity correlation function on fragment charge with details depending on the assumption with which momentum conservation constraints are implemented.

Uncertainties due to initial-state momentum conservation constraints can be significant for systems which disintegrate nearly instantaneously ($\tau \rightarrow 0$). For long-lived systems de-

caying via a sequence of binary emissions with complete reequilibration of the source between individual steps, the implementation of momentum conservation is *well defined* and the uncertainties discussed in this paper are unimportant. Extracted upper limits of sequential IMF emission time scales thus remain valid. However, evidence for a very fast sequential (as opposed to near-instantaneous) decay mechanism derived from energy-dependent two-fragment correlation functions may be more ambiguous than previously believed and may need further evaluation.

While calculations for instantaneous decay are, indeed, sensitive to details of the spatial decay configuration, the predicted effects are comparable in magnitude to the uncertainties which arise from unknown initial-state momentum correlations. Unless these initial-state momentum correlations can be constrained by new experimental observables or by *ab initio* dynamical calculations, it appears difficult to extract unambiguous information about the spatial configuration of an instantaneously disintegrating source.

[1] W. G. Lynch, Annu. Rev. Nucl. Part. Sci. **37**, 493 (1987), and references therein.

[2] L. G. Moretto and G. J. Wozniak, Annu. Rev. Nucl. Part. Sci. **43**, 379 (1993), and references therein.

[3] D. H. E. Gross, Rep. Prog. Phys. **53**, 605 (1990), and references therein.

[4] J. P. Bondorf *et al.*, Phys. Rep. **257**, 133 (1995), and references therein.

[5] A. S. Botvina *et al.*, Nucl. Phys. **A584**, 737 (1995).

[6] W. A. Friedman *et al.*, Phys. Rev. C **28**, 16 (1983).

[7] W. A. Friedman, Phys. Rev. Lett. **60**, 2125 (1988).

[8] W. A. Friedman, Phys. Rev. C **42**, 667 (1988).

[9] L. G. Moretto, K. Tso, N. Colonna, and G. J. Wozniak, Phys. Rev. Lett. **69**, 1884 (1992).

[10] W. Bauer, G. F. Bertsch, and H. Schulz, Phys. Rev. Lett. **69**, 1888 (1992).

[11] D. H. E. Gross, B. A. Li, and A. R. DeAngelis, Ann. Phys. (Leipzig) **1**, 467 (1992).

[12] B. Borderie, B. Remaud, M. F. Rivet, and F. Sebille, Phys. Lett. B **302**, 53 (1985).

[13] H. M. Xu *et al.*, Phys. Rev. C **48**, 933 (1993).

[14] D. O. Handzy *et al.*, Phys. Rev. C **50**, 858 (1994).

[15] M. Colonna, M. Di Toro, V. Latora, and A. Smerzi, Prog. Part. Nucl. Phys. **30**, 17 (1992).

[16] R. Trockel *et al.*, Phys. Rev. Lett. **59**, 2844 (1987).

[17] R. Bougault *et al.*, Phys. Lett. B **232**, 291 (1989).

[18] Y. D. Kim *et al.*, Phys. Rev. C **45**, 338 (1992); **45**, 387 (1992).

[19] D. R. Bowman *et al.*, Phys. Rev. Lett. **70**, 3534 (1993).

[20] T. Glasmacher *et al.*, Phys. Rev. C **50**, 952 (1994).

[21] D. Fox *et al.*, Phys. Rev. C **50**, 2424 (1994).

[22] D. R. Bowman *et al.*, Phys. Rev. C **52**, 818 (1995).

[23] E. Cornell *et al.*, Phys. Rev. Lett. **75**, 1475 (1995).

[24] T. M. Hamilton *et al.*, Phys. Rev. C **53**, 2273 (1996).

[25] Y. Lou *et al.*, Nucl. Phys. **A604**, 219 (1996).

[26] M. D'Agostino *et al.*, Phys. Lett. B **368**, 259 (1996).

[27] B. Kämpfer *et al.*, Phys. Rev. C **48**, R955 (1993).

[28] O. Schapiro, A. R. de Angelis, and D. H. E. Gross, Nucl. Phys. **A568**, 333 (1994).

[29] O. Schapiro and D. H. E. Gross, Nucl. Phys. **A573**, 143 (1994).

[30] M. D'Agostino *et al.*, Phys. Lett. B **371**, 175 (1996).

[31] T. Glasmacher, C. K. Gelbke, and S. Pratt, Phys. Lett. B **314**, 265 (1993).

[32] I. Iori *et al.*, Nucl. Instrum. Methods Phys. Res. A **325**, 458 (1993); M. Bruno *et al.*, *ibid.* **311**, 189 (1992); N. Colonna *et al.*, *ibid.* **321**, 529 (1992); P. F. Mastinu *et al.*, *ibid.* **338**, 419 (1994).

[33] R. T. de Souza *et al.*, Nucl. Instrum. Methods Phys. Res. A **295**, 109 (1990).

[34] L. Phair *et al.*, Nucl. Phys. **A548**, 489 (1992).

[35] M. A. Lisa *et al.*, Phys. Rev. C **44**, 2865 (1991).

[36] D. A. Brown and P. Danielewicz, Phys. Lett. B **398**, 252 (1997).

[37] Y. D. Kim *et al.*, Phys. Rev. Lett. **67**, 14 (1991).

[38] Emission times extracted from angle-integrated two-fragment correlation functions exhibit a space-time ambiguity [20]: a longer time scale is extracted if one assumes a smaller source, and a shorter time scale is extracted for a larger source.

[39] T. C. Awes and C. K. Gelbke, Phys. Rev. C **27**, 137 (1983).